

In situ preparation of g-C₃N₄/bismuth-based oxide nanocomposites with enhanced photocatalytic activity

Wenjie Shan, Yun Hu*, Zhaogao Bai, Mengmeng Zheng, Chaohai Wei

The Key Lab of Pollution Control and Ecosystem Restoration in Industry Clusters, Ministry of Education, School of Environment and Energy, South China University of Technology, Guangzhou 510006, PR China



ARTICLE INFO

Article history:

Received 16 November 2015

Received in revised form 22 January 2016

Accepted 24 January 2016

Available online 28 January 2016

Keywords:

g-C₃N₄

Bi₂O₂CO₃

BiOCl

Nanocomposite

Photoactivity

ABSTRACT

Different mass percents of g-C₃N₄/Bi₂O₂CO₃ and g-C₃N₄/BiOCl nanocomposites with intimately contacted interfaces were synthesized in situ by mixing Bi₂O₃ nanoparticles with melamine or guanidine hydrochloride and calcinating at 550 °C for 3 h. The fabricated nanocomposites were well-characterized by various analytical techniques. The results showed that the Bi₂O₂CO₃ and BiOCl nanosheets grow out from the g-C₃N₄ bulk, producing closely contacted interfaces between the Bi oxide component and the g-C₃N₄ component. The UV-vis diffuse reflectance spectra of g-C₃N₄/Bi₂O₂CO₃ and g-C₃N₄/BiOCl nanocomposites exhibited increased visible light absorption compared to g-C₃N₄ and Bi₂O₃ separately. Moreover, the nanocomposites showed significantly enhanced photocatalytic activity for the degradation of dibutyl phthalate and methyl orange under visible light. A proposed photocatalytic mechanism for the enhanced photoactivity of nanocomposites was investigated by scavenging experiments and fluorescent spectroscopy. The increased photocatalytic activity is mainly attributed to the effective separation and transfer of photo-induced carriers in the intimate contact between g-C₃N₄ and Bi₂O₂CO₃ or BiOCl. The results showed that the different precursors of g-C₃N₄ have a significant effect on the composite's structure; i.e., Bi₂O₃ can react to form different bismuth-based oxides depending on the different precursors used to generate g-C₃N₄. This work demonstrates a convenient way to fabricate visible light responsive materials with potential for environmental remediation.

© 2016 Elsevier B.V. All rights reserved.

1. Introduction

Dibutyl phthalate (DBP) is widely used in chemical industry, which is one of the most commonly used plasticizers. It has been detected in water, soils and environmental organisms in recent years. DBP has adverse effects on ecosystems because it can interfere with the endocrine system of humans or animals. Therefore, it is important to find an effective way to minimize the harm of DBP in environment. Semiconductor photocatalysis is a promising environmental remediation technology which can be used to treat the inorganic or organic pollutants in the environment [1,2]. To date, many semiconductor photocatalysts have been studied for use in water splitting and environmental remediation. Among them, TiO₂ is the most widely investigated semiconductor photocatalyst due to its high oxidation ability, good stability, low cost and low toxicity [3,4]. However, practical applications of TiO₂ are quite limited, because it only responds to the ultraviolet (UV) light, lacking any

visible light absorption [5]. Therefore, design and development of visible light responsive semiconductor photocatalysts have been significant research topics in recent years.

Bismuth-based semiconductors (e.g., Bi₂O₃, CaBi₂O₄, Bi₂WO₆, BiVO₄, Bi₄Ti₃O₁₂, Bi₂O₂CO₃ and BiOIO₃) have attracted much attention due to their many advantages, such as superior photocatalytic performance under UV and visible light irradiation, unique layered structures and resistance to photocorrosion, chemical stability, low/non-toxicity, and earth abundance [6–10]. Among the various bismuth-based semiconductors, bismuth oxide (Bi₂O₃) with a band gap varying from 2.0 to 3.96 eV is a strong candidate because of its properties that include good photoconductivity and significant visible light response [9–12]. Moreover, Bi₂O₃ reacts to form other bismuth-based oxides under certain conditions; e.g., Bi₂O₃ reacts to form BiOCl when treated with HCl [13] and reacts to form Bi₂O₂CO₃ in the presence of carbon sources [14]. However, pure Bi₂O₃ itself has been a bit of a disappointment as a photocatalyst due to the fast recombination of the photo-induced electrons and holes in the material. Much work is centered on methods by which Bi₂O₃ can be transformed into a more efficient visible light photocatalytic material.

* Corresponding author.

E-mail address: huyun@scut.edu.cn (Y. Hu).

Recently, graphitic carbon nitride ($\text{g-C}_3\text{N}_4$) has been an object of extensive research interest because of its chemical and photochemical stability, favorable optical absorption with a band gap of 2.7 eV and ease of fabrication from simple precursors (e.g., urea and melamine, among others) through a series of polycondensation reactions without any metal involvement [15–18]. Wang et al. first reported that $\text{g-C}_3\text{N}_4$ can be used for hydrogen production from water splitting under visible light illumination [19]. Some researchers have since reported that $\text{g-C}_3\text{N}_4$ can be successfully used for photocatalytic degradation of organic pollutants under visible light [15,20]. However, the low efficiency of $\text{g-C}_3\text{N}_4$ is still a problem, limiting its practical application because of the fast recombination of photo-induced carriers in the material [21]. Many efforts have been undertaken to overcome this problem, including metal or non-metal doping [22,23], nanoporous structure design, morphology control, and coupling with other semiconductors [24–28]. Constructing heterostructures through coupling $\text{g-C}_3\text{N}_4$ with other semiconductors is one approach for suppressing the recombination of photo-induced electrons-holes pairs and improving photocatalytic performance [24,29,30].

Therefore, based on the respective energy levels in Bi_2O_3 and $\text{g-C}_3\text{N}_4$, we have conducted this study into the coupling of the two semiconductors in search of efficient visible light responsive photocatalytic activity for DBP and dye degradations. Also, building on previous researches that have shown that the $\text{g-C}_3\text{N}_4$ materials prepared by different precursors present significant differences in specific surface area, morphology and photocatalytic activity [30], we have explored the effect of $\text{g-C}_3\text{N}_4$ prepared from different precursors on the structure and properties of composites of these $\text{g-C}_3\text{N}_4$ materials and Bi_2O_3 . Also, based on our results, a possible mechanism for the photocatalytic activity of these nanocomposites is proposed.

To the best of our knowledge, there are no published reports on such work.

2. Experimental

2.1. Materials

Melamine (Aladdin, AR), guanidine hydrochloride (Aladdin, AR), bismuth nitrate pentahydrate (SinoHarm Chemical Reagent Co.,Ltd, AR), nitric acid (Tianjin Chemical Reagent Factory, AR), sodium hydroxide (Tianjin Chemical Reagent Factory, AR) and methyl orange (Tianjin Chemical Reagent Factory, AR) were used as received. All other reagents used in this work were of AR grade.

2.2. Fabrication of materials

2.2.1. Preparation of Bi_2O_3 powder

The Bi_2O_3 samples were prepared using a precipitation method described in a previous report [32]. Briefly, 10.78 g of $\text{Bi}(\text{NO}_3)_3 \cdot 5\text{H}_2\text{O}$ was dissolved in 30 mL aqueous solution of HNO_3 (1.5 M). Then NaOH solution (50% w/v) was added dropwise under vigorous stirring until $\text{pH}=13$, at which point a yellow precipitate formed. Afterwards, the mixture was heated at 80 °C for 2 h. The obtained yellow precipitate was collected and washed with deionized water and ethanol several times before being dried at 100 °C for 12 h. Finally, the samples were calcined at 300 °C for 2 h using a heating rate of 2 °C/min to form the pure Bi_2O_3 powder.

2.2.2. Preparation of $\text{g-C}_3\text{N}_4$ and nanocomposites

The $\text{g-C}_3\text{N}_4$ was prepared by direct heating of a precursor (melamine or guanidine hydrochloride) to 550 °C for 3 h at a heating rate of 3 °C/min.

According to the previous reports, a general preparation method of $\text{g-C}_3\text{N}_4$ -containing compounds is putting the prepared $\text{g-C}_3\text{N}_4$

into the precursor of another semiconductor, then the semiconductor grows on the $\text{g-C}_3\text{N}_4$ surface, thus the composite material is obtained [24,25]. In our work, the nanocomposites were synthesized in situ by putting Bi_2O_3 powder into the precursor and heating at 550 °C for 3 h. Typically, a certain amount of Bi_2O_3 and 5 g of the precursor were added to absolute ethyl alcohol (the nominal contents of $\text{g-C}_3\text{N}_4$: 80, 60 and 40 wt%). A homogeneous suspension was obtained after stirring for 3 h and sonicating for 1 h. Finally, the samples were dried at 60 °C for overnight and next then calcined as described above for pure $\text{g-C}_3\text{N}_4$. In order to immobilize samples, the photocatalyst films were prepared by the doctor blade coating technique [33].

2.3. Characterizations

The crystal phase structures of the samples were identified by X-ray diffraction (XRD) (Bruker, D8) using $\text{Cu K}\alpha$ ($\lambda = 0.15418 \text{ nm}$) radiation. The scan range of 2θ was 10–80°. The morphology of samples was examined with field emission scanning electron microscopy (FE-SEM, Hitachi, S-4800) and transmission electron microscopy (TEM, JEOL, JEM-2010). UV-vis diffuse reflectance spectra (DRS) were recorded on a UV-vis spectrophotometer (Shimadzu, UV-2550) with BaSO_4 used as the reflectance standard. The specific surface areas of the calcined photocatalysts were measured on an Autosorb-1C-TCD physical adsorption instrument (Micromeritics, ASAP2010) by N_2 adsorption at 77 K. The specific surface areas were calculated using the Brunauer–Emmett–Teller (BET) method. Fourier transform infrared (FT-IR) spectra of solid samples were obtained on the Nicolet-6700 FT-IR spectrometer using KBr pellets. The binding energy was determined by X-ray photoelectron spectroscopy (XPS, Thermo Fisher Scientific, ESCALAB 250) with $\text{Al K}\alpha$ radiation. The XPS peaks were calibrated with the C 1s peaks derived from a surface contaminating hydrocarbon that had a binding energy of 284.8 eV.

2.4. Evaluation of photocatalytic activity

In the evaluation of the photocatalytic activity of the prepared samples, a 500 W halogen tungsten lamp with a 420 nm cut-off filter was used as the visible light source, and the light intensity was 1 mw/cm^2 , which was much weaker than that reported in other literatures [13,14]. Wavelength of incident light was 420–760 nm. DBP and methyl orange (MO) were used as representative pollutants to estimate the photocatalytic activity of the prepared samples, respectively. The photocatalytic degradations of DBP and MO were carried out in a home-made reactor to which a 0.1 g sample of photocatalyst was added to 100 mL of DBP solution (5 mg/L) or MO solution (20 mg/L). Before the irradiation process, the DBP or MO and catalyst suspension was stirred in dark for 30 min to reach adsorption-desorption equilibrium. At given time intervals, the DBP solution was estimated using high performance liquid chromatography after removing the catalysts from the dispersion by magnetic separation, or about 3 mL of the supernate resulting from centrifugation was collected and analyzed for MO using a UV-vis spectrometer. The characteristic absorption peak of MO at 464 nm was used to determine the extent of its degradation. The DBP or MO removal ratio (η) was calculated as $\eta (\%) = (1 - C/C_0) \times 100\%$, where C and C_0 are the concentrations of DBP or MO after and before reaction, respectively. Total organic carbon (TOC) assays were carried out on a Shimadzu TOC-V_{CPN} TOC analyzer.

2.5. Detection of reactive species

Different scavengers were subjected into the MO solution before adding the photocatalysts. The test method was similar to the photocatalytic experimental process.

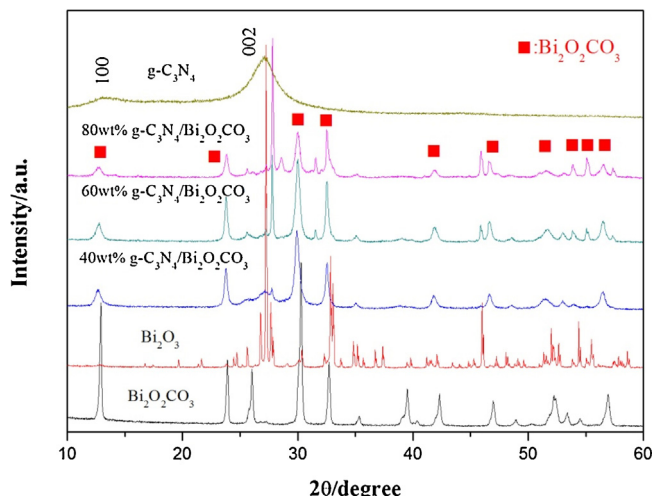


Fig. 1. XRD patterns of the prepared g-C₃N₄, Bi₂O₃, Bi₂O₂CO₃, and g-C₃N₄/Bi₂O₂CO₃ photocatalysts.

Also, the produced hydroxyl radical ($\cdot\text{OH}$) in the light irradiation process was measured by photoluminescence (PL) with terephthalic acid (TA) as a probe molecule. Briefly, 0.1g of sample was added to 100 mL of the TA solution (5×10^{-4} mol/L) containing with NaOH (2×10^{-3} mol/L) at room temperature. At 1 h intervals, the centrifuged supernate was measured with a PL spectrophotometer using an excitation wavelength of 420 nm.

3. Results and discussion

3.1. XRD analysis

The XRD patterns of g-C₃N₄, Bi₂O₃, Bi₂O₂CO₃, and g-C₃N₄/Bi₂O₂CO₃ photocatalysts are shown in Fig. 1. The diffraction peak at 27.7° of g-C₃N₄ is a characteristic interlayer stacking reflection of conjugated aromatic systems, which can be indexed to (002) diffraction planes [31]. The small peak at around 13.2° is indexed to (100) diffraction planes of g-C₃N₄ [34]. The main detectable diffraction peaks of Bi₂O₂CO₃ can be indexed to the tetragonal phase according to the PDF card (JCPDS 41-1488) [35]. Only the monoclinic phase of crystalline α -Bi₂O₃ is present in the prepared sample, which consistent with the result of JCPDS 71-2274 [36]. The sharp, well-separated diffraction peaks indicate that the samples were well-crystallized.

In the composite g-C₃N₄/Bi₂O₂CO₃ samples, the diffraction peaks of Bi₂O₂CO₃ were observed, while the diffraction peaks of Bi₂O₃ were reduced. These results indicate that the Bi₂O₂CO₃ was formed after the mixture of melamine and Bi₂O₃ were calcined at 550 °C. Taking into consideration the fact that Bi₂O₃ can be transformed to Bi₂O₂CO₃ in a CO₂ atmosphere and that melamine may produce large amounts of CO₂ gas during the g-C₃N₄ formation at high temperature, we infer that Bi₂O₃ reacted with CO₂ to form Bi₂O₂CO₃. Also, the XRD peak intensity of Bi₂O₂CO₃ increased and the diffraction peaks appeared to be sharpen as the amount of Bi₂O₃ input is increased. In addition, some small XRD peaks of Bi₂O₃ were observed in the composites, suggesting that there were small amount of Bi₂O₃ residues in the composites.

A g-C₃N₄ composite was obtained when a mixture of Bi₂O₃ and guanidine hydrochloride (CH₅N₃·HCl) were calcined at 550 °C. Previous studies have shown that in the presence of HCl, Bi₂O₃ can react to form BiOCl [13]. The XRD results of that composite are shown in Fig. 2, providing evidence of g-C₃N₄/BiOCl, suggesting that the Bi₂O₃ reacted with HCl produced by CH₅N₃·HCl during the g-C₃N₄ formation.

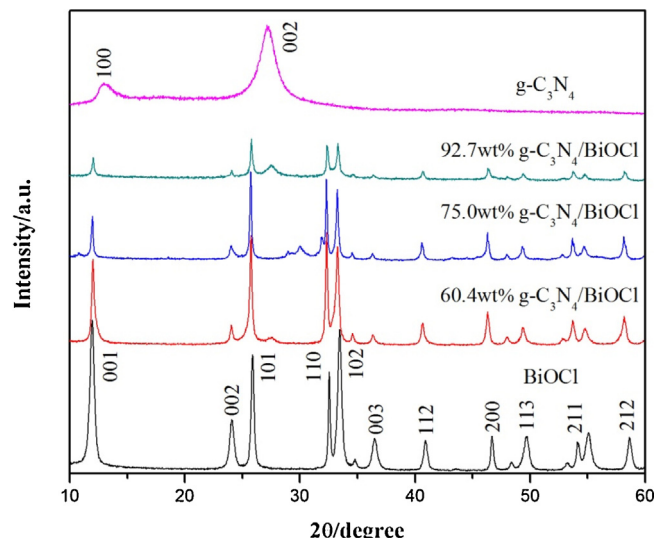


Fig. 2. XRD patterns of different catalysts.

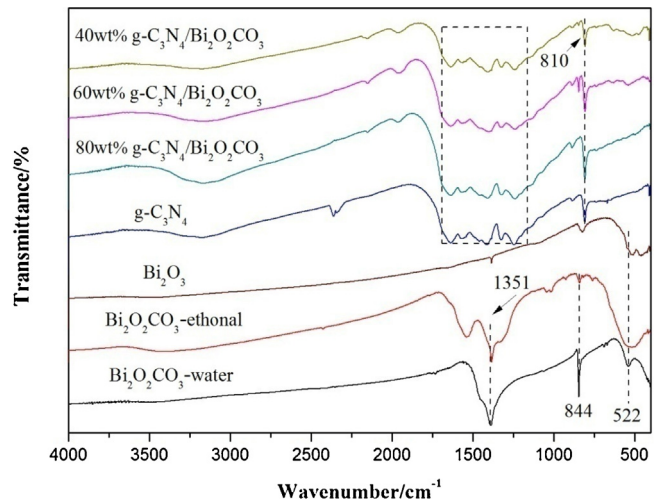


Fig. 3. FT-IR spectra of the prepared g-C₃N₄, Bi₂O₃, Bi₂O₂CO₃, and g-C₃N₄/Bi₂O₂CO₃ samples.

In neither Figs. 1 nor 2 were there any obvious diffraction peaks of g-C₃N₄ observed in the composites, which may be explained by the fact that the peaks were concealed by other diffraction peaks, such as Bi₂O₂CO₃ and BiOCl.

3.2. FT-IR spectra analysis

Fig. 3 shows the FT-IR spectra of the prepared g-C₃N₄, Bi₂O₃, Bi₂O₂CO₃, and g-C₃N₄/Bi₂O₂CO₃ samples. The peak at around 522 cm⁻¹ is assigned to the stretching mode of Bi—O groups in Bi₂O₃ or Bi₂O₂CO₃. The peaks at 1351 and 844 cm⁻¹ are ascribed to the stretching modes of CO₃²⁻ groups in Bi₂O₂CO₃ [37]. In the FT-IR spectra of g-C₃N₄, the peaks in the region from 1200 to 1600 cm⁻¹ are ascribed to the typical stretching vibrations of CN heterocycles [34]. These peaks are also present in the g-C₃N₄/Bi₂O₂CO₃ composites, suggesting that g-C₃N₄ exists in the composites. The peak at 810 cm⁻¹ is attributed to the characteristic breathing mode of s-triazine [26], which increases with the increase of the g-C₃N₄ content.

From the results of XRD and FT-IR analyses, it can be seen that Bi₂O₃ reacted to form different bismuth-based oxides in the presence of different g-C₃N₄ precursors; i.e., Bi₂O₃ formed Bi₂O₃CO₃

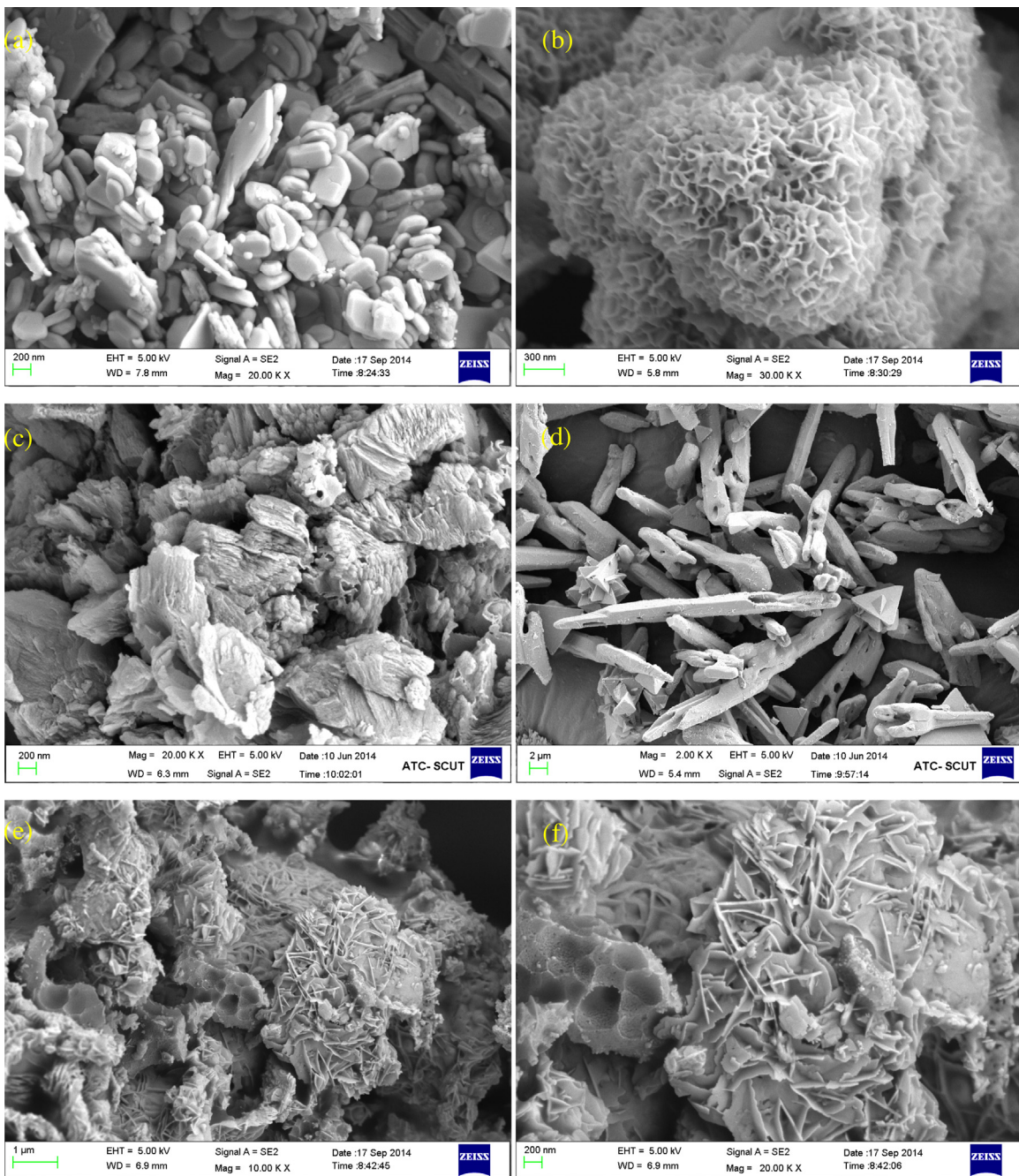


Fig. 4. FE-SEM images of (a) $\text{Bi}_2\text{O}_2\text{CO}_3$ -water; (b) $\text{Bi}_2\text{O}_2\text{CO}_3$ -ethanol; (c) $\text{g-C}_3\text{N}_4$; (d) Bi_2O_3 and (e) $\text{g-C}_3\text{N}_4/\text{Bi}_2\text{O}_2\text{CO}_3$; (f) magnified FE-SEM image of $\text{g-C}_3\text{N}_4/\text{Bi}_2\text{O}_2\text{CO}_3$.

and BiOCl in the presence of melamine and guanidine hydrochloride, respectively.

3.3. Morphological analysis

The morphology and nanostructure of the prepared samples were characterized by FE-SEM and TEM measurements. Fig. 4a and b shows the morphologies of two different samples of $\text{Bi}_2\text{O}_2\text{CO}_3$ prepared using water and ethanol as the solvent, respectively. The $\text{Bi}_2\text{O}_2\text{CO}_3$ -water sample displayed a flake-like nanostructure with a thickness of about 50–100 nm and the size of several hundred nanometers. In contrast, the $\text{Bi}_2\text{O}_2\text{CO}_3$ -ethanol sample exhibited a flower-like microsphere which consisted of thin flakes, indicating that the microstructure is affected by using different solvents.

Fig. 4c shows that the pure $\text{g-C}_3\text{N}_4$ had a typically aggregated morphology with a layered structure and a large size. Interestingly, some thin flakes sprouted from the blocky structure in the composites (Fig. 3e and f) after the mixture of melamine and Bi_2O_3 was calcined, while the rod-like structures of Bi_2O_3 (Fig. 3d) cannot be observed. A similar phenomenon occurred in the $\text{g-C}_3\text{N}_4/\text{BiOCl}$ composite prepared by heating the mixture of Bi_2O_3 and $\text{CH}_5\text{N}_3\cdot\text{HCl}$, as shown in Fig. S1. These results suggest that the $\text{Bi}_2\text{O}_2\text{CO}_3$ flower-like thin flakes were formed in the composites due to the transformation of Bi_2O_3 in the presence of CO_2 , which are consistent with the XRD and FT-IR measurements.

In summary, SEM images show that the $\text{g-C}_3\text{N}_4/\text{Bi}_2\text{O}_2\text{CO}_3$ and $\text{g-C}_3\text{N}_4/\text{BiOCl}$ composites can be synthesized by the in-situ calcina-

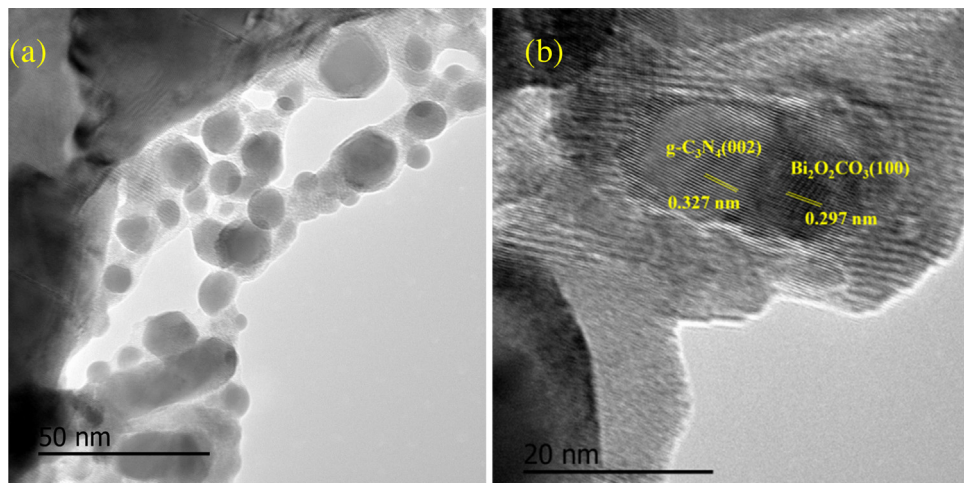


Fig. 5. (a) TEM image and (b) HR-TEM image of the 60 wt% $\text{g-C}_3\text{N}_4/\text{Bi}_2\text{O}_2\text{CO}_3$ composite.

Table 1
The BET specific surface area of different catalysts.

Samples	Specific surface area ($\text{m}^2 \text{g}^{-1}$)
$\text{g-C}_3\text{N}_4$	6.71
Bi_2O_3	8.95
$\text{Bi}_2\text{O}_2\text{CO}_3$	15.35
BiOCl	12.34
$\text{g-C}_3\text{N}_4/\text{Bi}_2\text{O}_2\text{CO}_3$	25.01
$\text{g-C}_3\text{N}_4/\text{BiOCl}$	25.50

tion method with the result that the fundamental components of $\text{g-C}_3\text{N}_4$ and $\text{Bi}_2\text{O}_2\text{CO}_3$ and BiOCl , respectively, are in close contact.

Fig. 5 shows the TEM images of 60 wt% $\text{g-C}_3\text{N}_4/\text{Bi}_2\text{O}_2\text{CO}_3$ composites. As can be seen from Fig. 5a, the $\text{Bi}_2\text{O}_2\text{CO}_3$ contacts closely with the $\text{g-C}_3\text{N}_4$; i.e., almost no $\text{Bi}_2\text{O}_2\text{CO}_3$ thin flakes can be observed outside the $\text{g-C}_3\text{N}_4$ nanosheets. The HR-TEM in Fig. 5b clearly shows the lattice fringes of 0.327 nm that are ascribed to the (002) plane of $\text{g-C}_3\text{N}_4$ and the lattice fringes of 0.297 nm that correspond to the (100) plane of tetragonal $\text{Bi}_2\text{O}_2\text{CO}_3$ [38].

Therefore, the SEM and TEM results show that the $\text{g-C}_3\text{N}_4/\text{Bi}_2\text{O}_2\text{CO}_3$ composite was successfully prepared by in-situ growth mechanism and that the components are in close contact. Taking into consideration that this close contact between the two components in composite materials should be beneficial to the transfer of photo-induced carriers [39], the $\text{g-C}_3\text{N}_4/\text{Bi}_2\text{O}_2\text{CO}_3$ and $\text{g-C}_3\text{N}_4/\text{BiOCl}$ nanocomposites prepared by the in-situ synthesis method are expected to show enhanced photocatalytic activity.

3.4. BET analysis

Table 1 presents the specific surface area of the samples. Compared with the pure catalysts, the composite photocatalysts $\text{g-C}_3\text{N}_4/\text{Bi}_2\text{O}_2\text{CO}_3$ and $\text{g-C}_3\text{N}_4/\text{BiOCl}$ showed larger specific surface areas, which were 25.01 and $25.50 \text{ m}^2 \text{ g}^{-1}$, respectively. This was caused by the gas generated during the thermal polymerization process.

3.5. XPS analysis

XPS analysis was performed to investigate the chemical composition of $\text{g-C}_3\text{N}_4/\text{Bi}_2\text{O}_2\text{CO}_3$ composites. The high resolution spectra of Bi 4f, O 1s, C 1s and N 1s are shown in Fig. 6. The binding energy for C1s peak at 284.8 eV was used as a reference. The binding energies at 164.01 and 158.7 eV of pure Bi_2O_3 are attributed to $\text{Bi4f}_{5/2}$ and $\text{Bi4f}_{7/2}$, respectively [36]. However, the binding energies

shifted to 164.81 and 159.49 eV in the composites, corresponding to the $\text{Bi4f}_{5/2}$ and $\text{Bi4f}_{7/2}$ of $\text{Bi}_2\text{O}_2\text{CO}_3$, respectively [40]. Similarly, the peaks of O 1s were also changed, and the binding energy was changed from 529.26 eV to 530.61 eV, which is attributed to the $[\text{Bi}_2\text{O}_2]^{2+}$ in $\text{Bi}_2\text{O}_2\text{CO}_3$ [40]. The peak at 530.51 eV is characteristic of Bi-O binding energy in Bi_2O_3 , and the peak at 531.62 eV is attributed to Bi-O in $\text{Bi}_2\text{O}_2\text{CO}_3$. These results show that the $\text{Bi}_2\text{O}_2\text{CO}_3$ was formed in the composites.

In Fig. 6c, the peaks of C 1s binding energies at 284.81 and 288.39 eV can be assigned to carbon atoms (C-C bonding) in a carbon environment; i.e., amorphous carbon adsorbed on the surface and carbon atoms bond in N-containing aromatic rings (N-C=N), respectively. Fig. 6d is a high resolution spectrum of N 1s. Three peaks can be distinguished at 398.80, 399.89 and 401.33 eV. The binding energies at 398.80 and 401.33 eV belong to sp^2 -bonded N in the triazine rings (C-N=C) and amino groups (C-N-H), respectively [41]. The peak at 399.89 eV was assigned to the tertiary nitrogen in the form of N-(C)₃ groups. The tiny peak at 404.8 eV was ascribed to the charging effects or positive charge localization in the heterocycles [41–44].

In short, the XPS results indicated that both $\text{g-C}_3\text{N}_4$ with graphite-like sp^2 -bonded structure and $\text{Bi}_2\text{O}_2\text{CO}_3$ existed in the composite. The shifts of the peaks in the composite, compared with those in the pure $\text{g-C}_3\text{N}_4$, were attributed to the interaction between $\text{g-C}_3\text{N}_4$ and $\text{Bi}_2\text{O}_2\text{CO}_3$.

3.6. UV-vis DRS analysis

The UV-vis DRS spectra of the synthesized samples are shown in Fig. 7. The $\text{g-C}_3\text{N}_4$ exhibited absorption edges at around 460 nm in the visible range. The optical absorption band of the $\text{Bi}_2\text{O}_2\text{CO}_3$ -water sample presented a steep absorption edge only in the UV region. However, the $\text{Bi}_2\text{O}_2\text{CO}_3$ -ethanol sample with its flower-like structure exhibited an enhanced absorption in the visible region. These data show that the optical absorption and band gap energy are affected by the morphology of $\text{Bi}_2\text{O}_2\text{CO}_3$, which is consistent with previous reports [45]. With the increase of Bi_2O_3 dosage, the absorption edge of the composites showed a red shift. That is, with increasing $\text{Bi}_2\text{O}_2\text{CO}_3$ content, the composites had a wider range of UV-vis absorption close to that of $\text{Bi}_2\text{O}_2\text{CO}_3$ -ethanol, suggesting that the structure and photochemical property of $\text{Bi}_2\text{O}_2\text{CO}_3$ in $\text{g-C}_3\text{N}_4/\text{Bi}_2\text{O}_2\text{CO}_3$ is similar to that of the $\text{Bi}_2\text{O}_2\text{CO}_3$ -ethanol sample. This conjecture is consistent with the SEM results. Moreover, the color of the films fixed on the glass gradually changed from pale yellow to brown with the increase in the $\text{Bi}_2\text{O}_2\text{CO}_3$ content, as shown

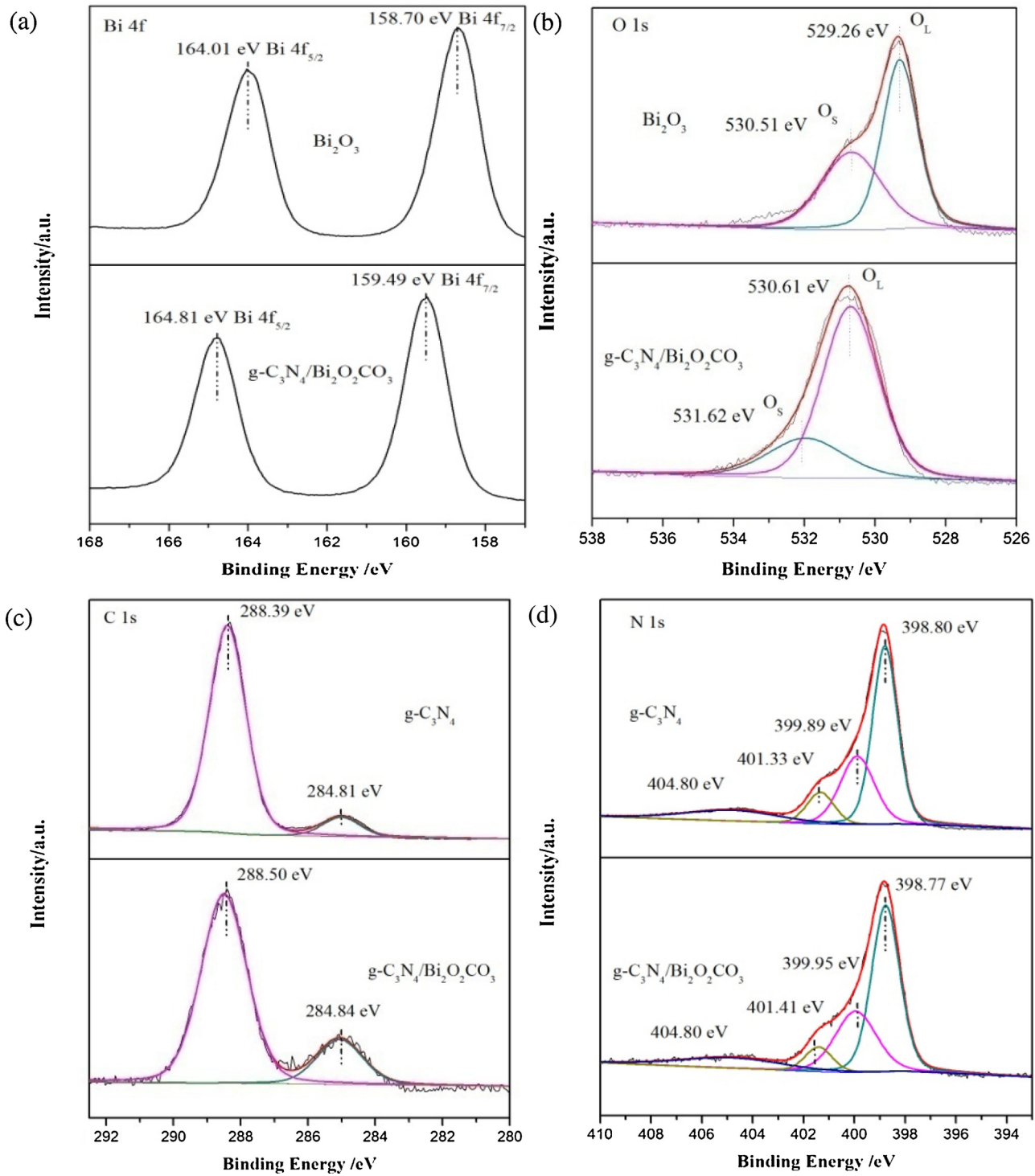


Fig. 6. High resolution XPS spectra of (a) Bi 4f, (b) O 1s, (c) C 1s and (d) N 1s.

in Fig. 7a. Similarly, the $\text{g-C}_3\text{N}_4/\text{BiOCl}$ nanocomposite also had a wide range of visible light response, as shown in Fig. S2.

In general, for a crystalline semiconductor, the optical absorption band edge can be estimated according to the formula $(\alpha h\nu)^n = A(h\nu - E_g)$, where α , h , ν , A and E_g are, respectively, the absorption coefficient, Plank's constant, light frequency, a constant and band gap [46]. The value of n is 2 for the direct transition and 1/2 for the indirect transition. For $\text{Bi}_2\text{O}_2\text{CO}_3$, the value of n is 1/2 for the indirect transition, thus the band gaps were estimated to be about 3.38 eV for $\text{Bi}_2\text{O}_2\text{CO}_3$ -water and 2.55 eV for $\text{Bi}_2\text{O}_2\text{CO}_3$ -ethanol, as

shown in Fig. 6c. By similar analysis, the optical band gap for $\text{g-C}_3\text{N}_4$ was estimated to be about 2.72 eV.

In addition, the potentials of the valence band (VB) and conduction band (CB) for $\text{Bi}_2\text{O}_3\text{CO}_3$ crystal can be calculated according to the two formulas which are proposed by Butler and Ginley:

$$E_{\text{VB}} = X - E_e + 0.5 E_g$$

$$E_{\text{CB}} = E_{\text{VB}} - E_g,$$

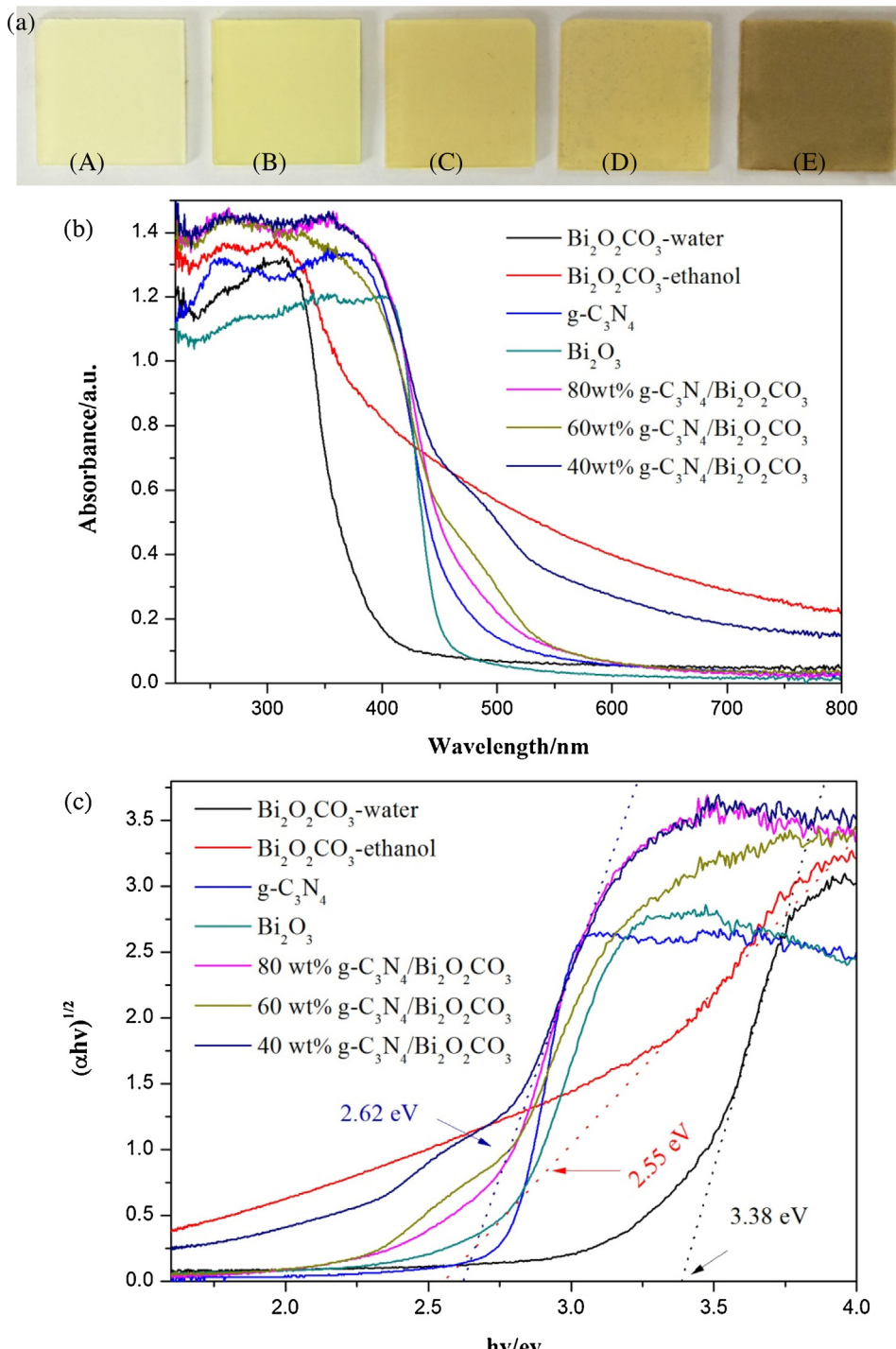


Fig. 7. (a) Photographs of the thin films: (A) Bi_2O_3 , (B) $\text{g-C}_3\text{N}_4$, (C) 80 wt% $\text{g-C}_3\text{N}_4/\text{Bi}_2\text{O}_3\text{CO}_3$, (D) 60 wt% $\text{g-C}_3\text{N}_4/\text{Bi}_2\text{O}_3\text{CO}_3$, (E) 40 wt% $\text{g-C}_3\text{N}_4/\text{Bi}_2\text{O}_3\text{CO}_3$; (b) UV-vis spectra of different catalysts; (c) $(\alpha h\nu)^{1/2}$ vs. $h\nu$ curves of different catalysts. (For interpretation of the references to color in the text, the reader is referred to the web version of this article.)

where E^e is the energy of free electrons on the hydrogen scale (that is, 4.5 eV); X is the absolute electronegativity of the corresponding semiconductor material; and E_{VB} , E_{CB} and E_g are the VB potential, CB potential and band gap of semiconductor material, respectively [47]. The X value of $\text{Bi}_2\text{O}_3\text{CO}_3$ was calculated to be 6.36 eV. Based on the above formulas, the VB potential and CB potential of $\text{Bi}_2\text{O}_3\text{CO}_3$ were calculated to be 3.13 eV and 0.58 eV, respectively.

3.7. Photocatalytic performance

The photocatalytic activities of the samples were evaluated by photocatalytic degradation of a MO solution under visible light. As shown in Fig. 8a, the characteristic absorption band of MO at 464 nm decreased significantly with increasing irradiation time, indicating the destruction of the conjugated structure [48]. The reduction in the absorption band at 270 nm was attributed to the ring cleavage reaction of the benzene ring. These absorption peaks disappeared

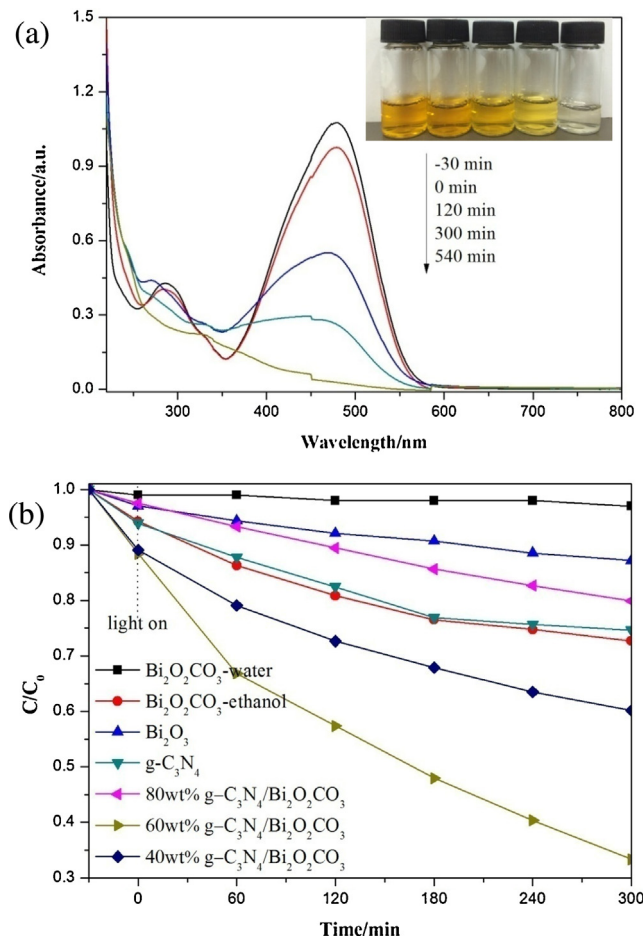


Fig. 8. (a) UV-vis spectrum changes of the MO degradation by the $\text{g-C}_3\text{N}_4/\text{Bi}_2\text{O}_2\text{CO}_3$ catalyst; (b) the photocatalytic degradation of MO by different $\text{g-C}_3\text{N}_4/\text{Bi}_2\text{O}_2\text{CO}_3$ catalysts under visible light.

completely after irradiation for 9 h, reflecting the complete decolorization of the MO solution as shown in the inset of Fig. 8a.

For simplicity, the absorption of MO at 464 nm was used to estimate the degradation of MO, as shown in Fig. 8b. The blank (i.e., no photocatalyst) demonstrated that MO was stable under visible light irradiation for 300 min (shown in Fig. S3). The ability of the catalysts to adsorb MO (and thereby falsely imply degradation) was investigated in the dark for 60 min before the light was turned on. It can be seen that the MO and catalyst suspension reached absorption-desorption equilibrium at 30 min (Fig. S3). The results showed that only small amount of organic pollutants were adsorbed on the composite, indicating that the catalysts were poor adsorbents for MO.

The pure $\text{g-C}_3\text{N}_4$ and pure Bi_2O_3 exhibited generally low photocatalytic activity, with only 24% and 13% MO degradation, respectively, after visible light irradiation for 300 min. Further, only 28% of MO was eliminated by $\text{Bi}_2\text{O}_2\text{CO}_3$ -ethanol under the same conditions. This low performance is likely due to the fast recombination of photo-induced electrons and holes in the single semiconductor. However, these three photocatalysts showed higher activities than $\text{Bi}_2\text{O}_2\text{CO}_3$ -water, due to their visible light response.

Among the nanocomposites, the highest activity was obtained with the 60 wt% $\text{g-C}_3\text{N}_4/\text{Bi}_2\text{O}_2\text{CO}_3$ sample, with which almost 70% of MO was degraded within 300 min. A pseudo-first order kinetic equation $-\ln(C/C_0)=kt$ produced a good fit to the experimental data, as shown in Fig. S4. The results indicated that the rate constant k was 0.00249 min^{-1} , which is about 6.3 and 2.8 times

greater than the rate constants displayed by pure $\text{g-C}_3\text{N}_4$ and Bi_2O_3 catalysts, respectively. $\text{g-C}_3\text{N}_4/\text{BiOCl}$ also showed greater photocatalytic activity than the pure $\text{g-C}_3\text{N}_4$ or Bi_2O_3 samples, as shown in Figs. 9 and S5. The enhanced photocatalytic activity of the composites may be due to the change of Bi_2O_3 into $\text{Bi}_2\text{O}_2\text{CO}_3$ or BiOCl in the presence of different $\text{g-C}_3\text{N}_4$ precursors during the synthesis process. In addition, the energy bands of generated $\text{Bi}_2\text{O}_2\text{CO}_3$ or BiOCl are well matched with $\text{g-C}_3\text{N}_4$.

Moreover, the degradation of DBP using different catalysts under visible light illumination was carried out. As shown in Fig. 10, almost 60% of DBP was degraded within 300 min, which was more efficient in the $\text{g-C}_3\text{N}_4/\text{Bi}_2\text{O}_2\text{CO}_3$ or $\text{g-C}_3\text{N}_4/\text{BiOCl}$ dispersion as compared to any single catalyst. This is similar with the results of MO degradation. The results indicated that the nanocomposites can effectively remove organic pollutants. In order to further assess the mineralization of DBP in water, TOC was monitored during the reaction process. Fig. S6 depicts the TOC removal after 4 h of visible light irradiation with the composite photocatalysts. The mineralization rates of organic carbon in MO and DBP were 48% and 43% on 75 wt% $\text{g-C}_3\text{N}_4/\text{BiOCl}$, while those were 45% and 38% on 60 wt% $\text{g-C}_3\text{N}_4/\text{Bi}_2\text{O}_2\text{CO}_3$, respectively. Compared to the degradation rate of MO and DBP, it can be seen that most of the organic molecules were mineralized in the photocatalytic degradation process.

The stability of composite photocatalyst was investigated by performing recycle experiments with 75 wt% $\text{g-C}_3\text{N}_4/\text{BiOCl}$ catalyst under visible light irradiation (Fig. 11). After four recycles, the photocatalytic activity did not show any obvious decay, demonstrating the high stability of the composite.

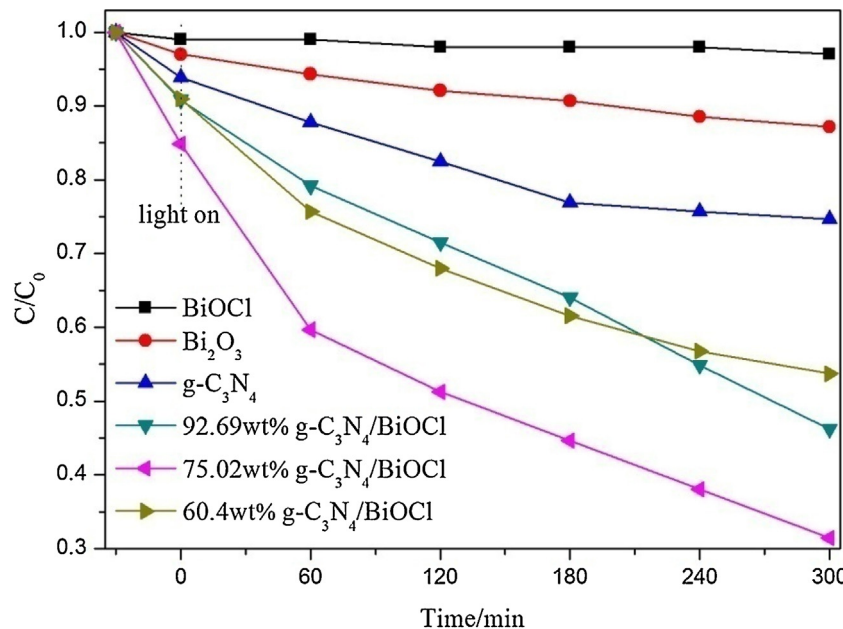


Fig. 9. The photocatalytic degradation of MO by different $g\text{-C}_3\text{N}_4/\text{BiOCl}$ catalysts under visible light.

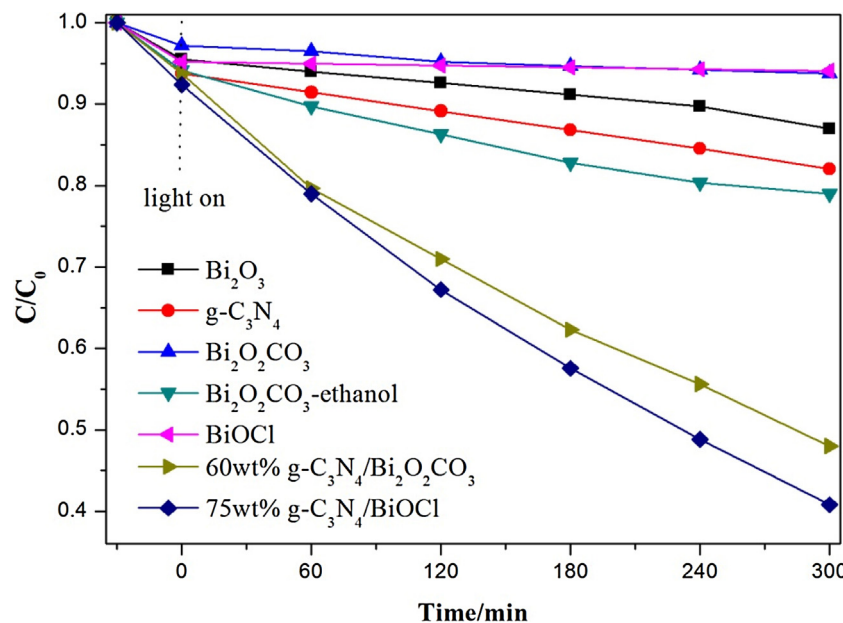


Fig. 10. The photocatalytic degradation of DBP by different photocatalysts under visible light.

Based on these experimental results, it can be inferred that the interfacial charge transfer between the two materials with the well-matched band structures and the closely contacted interfaces, which could enhance the separation of photo-induced carriers, are the main reasons for the enhanced photocatalytic activity.

3.8. Proposed photocatalytic mechanism

It is important to investigate the active species in the photocatalytic process in order to understand the mechanism of photocatalysis. In general, many active species, including $\cdot\text{OH}$, h^+ and $\cdot\text{O}_2^-$, can be expected to exist in a photocatalytic process. In this case, isopropanol (IPA), triethanolamine (TEOA) and N_2 purging were used as $\cdot\text{OH}$, h^+ and $\cdot\text{O}_2^-$ scavengers, respectively. As shown in Fig. 12, the photocatalytic activity of $g\text{-C}_3\text{N}_4/\text{Bi}_2\text{O}_2\text{CO}_3$

nanocomposite was greatly suppressed after the addition of TEOA, suggesting that h^+ was the main reactive species. Similarly, the obvious decrease in the photocatalytic activity observed by the addition of IPA and N_2 purging, respectively, suggested that $\cdot\text{OH}$ and $\cdot\text{O}_2^-$ play an important role in the reaction process, too. Formation of $\cdot\text{OH}$ in the reaction process can be measured by photoluminescence (PL) with the terephthalic acid (TA) as a probe molecule [49]. As shown in Fig. 13a, the intensity of PL spectra of $g\text{-C}_3\text{N}_4$ gradually increased with the illumination time, indicating the formation of $\cdot\text{OH}$ radicals. For $g\text{-C}_3\text{N}_4$, the CB potential (-1.15 eV) is more negative than the standard redox potential of $\text{O}_2/\cdot\text{O}_2^-$ (-0.046 eV), so the electrons in the CB can reduce the O_2 to $\cdot\text{O}_2^-$ and further react to form $\cdot\text{OH}$. Also, the VB potential ($+1.57\text{ eV}$) is more negative than the standard redox potentials of $\cdot\text{OH}/\text{OH}^-$ ($+1.99\text{ eV}$), so the holes on the VB cannot oxidize the OH^- to $\cdot\text{OH}$. These data

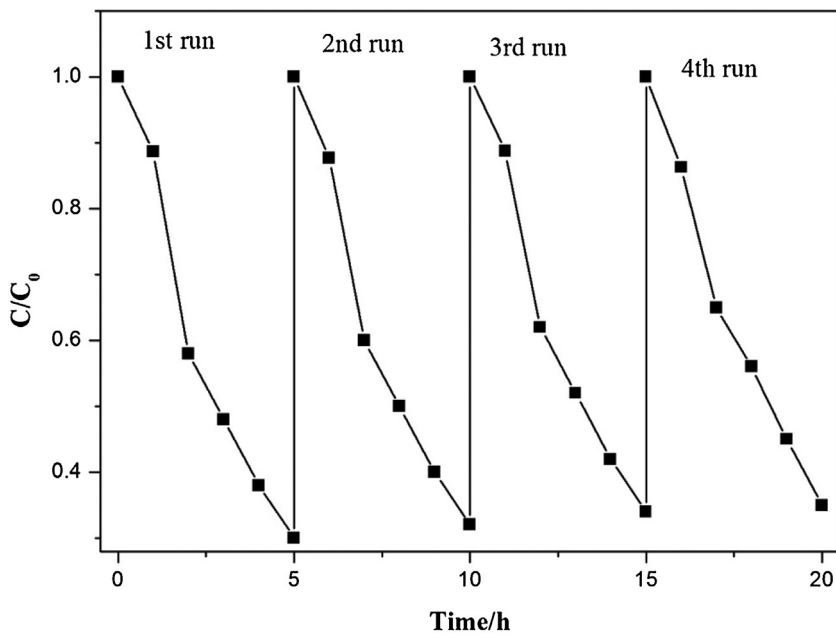


Fig. 11. Cycles of MO degradation over 75 wt% g-C₃N₄/BiOCl under visible light irradiation.

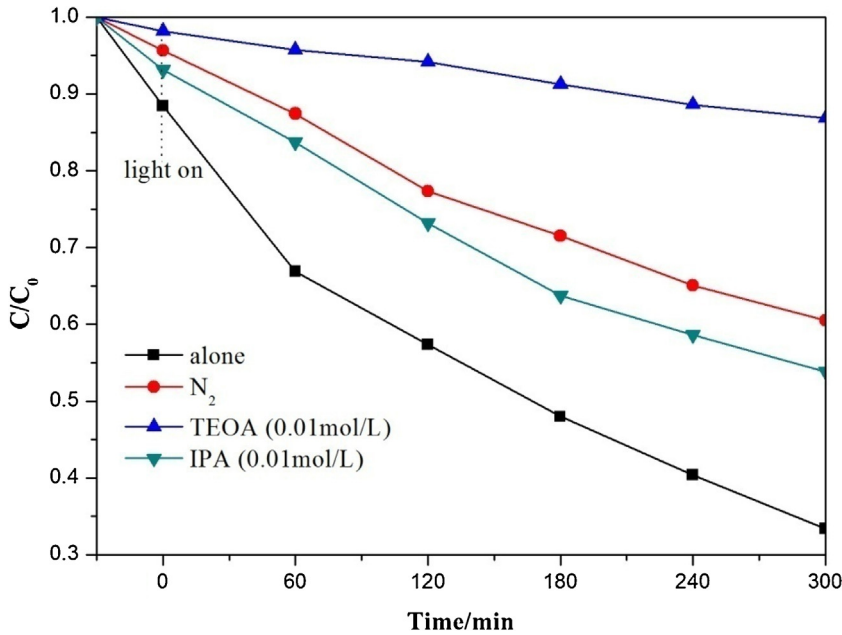


Fig. 12. Photocatalytic degradation of MO over 60 wt% g-C₃N₄/Bi₂O₂CO₃ as well as the addition of different scavengers.

suggest that •OH cannot be generated from the VB of g-C₃N₄, but it can be formed from the electrons on the CB of g-C₃N₄ [50]. According to an earlier report, the photo-induced holes in Bi₂O₂CO₃ cannot oxidize OH⁻ to form •OH, since the oxidation potential of holes in Bi₂O₂CO₃ depends on the standard redox potential of Bi^V/Bi^{III} (1.59 eV), which is more negative than the standard redox potential of •OH/OH⁻ (1.99 eV) [51]. Actually, the •OH radicals were not formed in the Bi₂O₂CO₃ system because no change of PL intensity is observed with increased irradiation time, as shown in Fig. 13b.

For the g-C₃N₄/Bi₂O₂CO₃ system, if the excited electrons in CB of g-C₃N₄ transfer to Bi₂O₂CO₃, the intensity of PL spectra of the composite would be lower than that of pure g-C₃N₄. As expected, it was found that the PL intensity of g-C₃N₄/Bi₂O₂CO₃ decreased compared to g-C₃N₄ (Fig. 13c). This result indicates that fewer

•OH radicals were formed in the g-C₃N₄/Bi₂O₂CO₃ system and the excited electrons in CB of g-C₃N₄ transferred to the CB of Bi₂O₂CO₃ based on the principle of thermodynamics, since the CB potential of g-C₃N₄ (-1.15 eV) is more negative than that of Bi₂O₂CO₃ (0.58 eV).

Based on these experimental and theoretical calculation results, a possible photocatalytic mechanism for degradation of MO by the g-C₃N₄/Bi₂O₂CO₃ nanocomposites proposed and is depicted in the schematic diagram in Fig. 14. Because of the well-matched band structure of g-C₃N₄/Bi₂O₂CO₃ and closely contacted interface, the excited electrons in the CB of g-C₃N₄ transfer to the CB of Bi₂O₂CO₃, the holes in the VB of Bi₂O₂CO₃ transfer to the VB of g-C₃N₄, under visible light irradiation. The holes in the VB of g-C₃N₄ can decompose MO directly, and the residual electrons in the CB of g-C₃N₄ can reduce O₂ to form •O₂⁻ or react with OH⁻ to form •OH radicals,

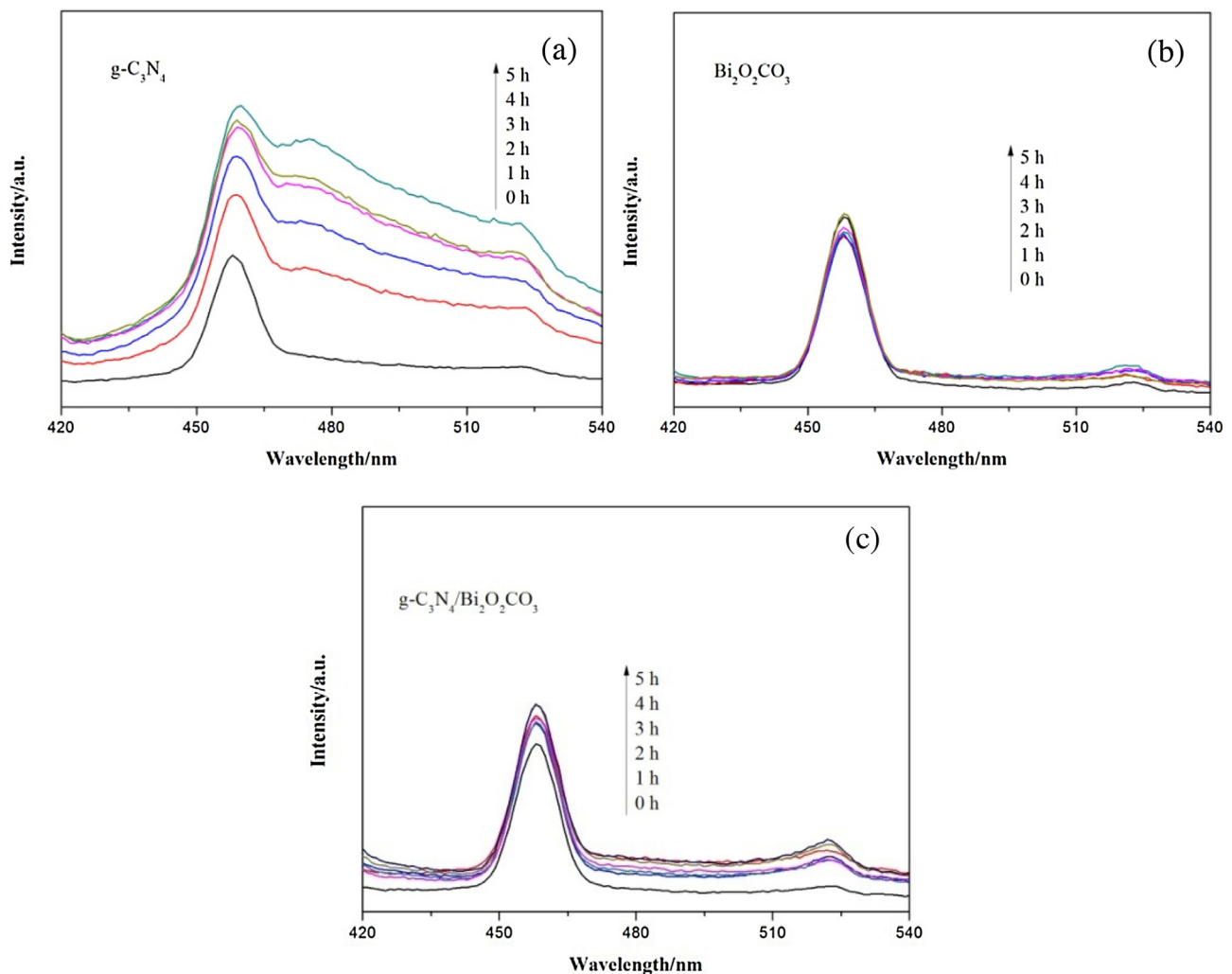


Fig. 13. PL spectra of (a) $\text{g-C}_3\text{N}_4$, (b) $\text{Bi}_2\text{O}_2\text{CO}_3$ and (c) $\text{g-C}_3\text{N}_4/\text{Bi}_2\text{O}_2\text{CO}_3$ in TA solution under visible light irradiation.

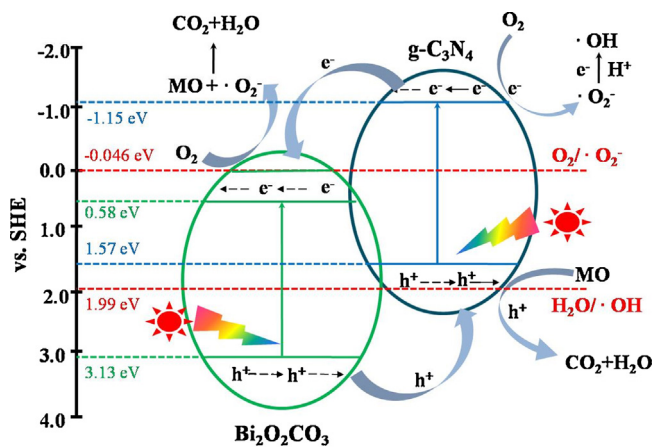


Fig. 14. The photocatalytic degradation mechanism of MO over $\text{g-C}_3\text{N}_4/\text{Bi}_2\text{O}_2\text{CO}_3$.

both of which can oxidize MO. The photogenerated electrons of the $\text{g-C}_3\text{N}_4$ transfer to a higher CB of $\text{Bi}_2\text{O}_2\text{CO}_3$ (potential more negative than $\text{O}_2/\text{•O}_2^-$ (-0.046 eV)) whose electrons can reduce O_2 to •O_2^- and further decompose MO. This phenomenon was reported in the $\text{g-C}_3\text{N}_4/\text{BiOBr}$ [51]. Thus, the photo-induced electrons and holes were separated effectively, and the surface electrons and holes could carry out the reduction and oxidation reactions, respectively.

In summary, the enhanced photocatalytic activity of $\text{g-C}_3\text{N}_4/\text{Bi}_2\text{O}_2\text{CO}_3$ was ascribed to the effective separation of photo-induced electrons and holes, facilitated by the closely connected interface. Similarly, the enhanced photocatalytic activity based on the above reasons can be observed in the $\text{g-C}_3\text{N}_4/\text{BiOCl}$ system which is prepared by the in-situ crystal growth mechanism, as shown in Fig. S5.

These data further support the conclusion that the in-situ growth mechanism is an effective method to design high-efficiency materials for environmental remediation.

4. Conclusions

$\text{G-C}_3\text{N}_4/\text{Bi}_2\text{O}_2\text{CO}_3$ and $\text{g-C}_3\text{N}_4/\text{BiOCl}$ nanocomposites were successfully synthesized using a simple in-situ crystal composite growth mechanism by heating the mixture of Bi_2O_3 and melamine or guanidine hydrochloride. The prepared nanocomposites exhibited enhanced photocatalytic activities under visible light. The effective separation of photo-induced carriers and the intimately contacted interface of $\text{g-C}_3\text{N}_4$ and $\text{Bi}_2\text{O}_2\text{CO}_3$ or BiOCl are the main reasons for the significant enhancements.

This work shows that the different precursors of $\text{g-C}_3\text{N}_4$ significantly affect the composites in regard to the morphology, visible light response and photocatalytic activity. In so doing, the study demonstrates a new strategy for the design and development of high-efficiency visible-light-driven photocatalysts with potential

applications for environmental remediation and clean energy production.

Acknowledgements

This work was supported by National Natural Science Foundation of China (21277051, 21577039), Science and Technology Planning Project of Guangdong Province, China (2015A020215004), and Science and Technology Planning Project of Guangzhou City, China (12C62081602). We are grateful for the language help provided by Dr. Donald G. Barnes.

Appendix A. Supplementary data

Supplementary data associated with this article can be found, in the online version, at <http://dx.doi.org/10.1016/j.apcatb.2016.01.058>.

References

- [1] M.R. Hoffmann, S.T. Martin, C. Wonyong, D.W. Bahnemann, *Chem. Rev.* 95 (1995) 69–96.
- [2] X.B. Chen, S.H. Shen, L.J. Guo, S.S. Mao, *Chem. Rev.* 110 (2010) 6503–6570.
- [3] K. Mori, H. Yamashita, M. Anpo, *RSC Adv.* 2 (2012) 3165–3172.
- [4] J. Schneider, M. Matsuoka, M. Takeuchi, J. Zhang, Y. Horiuchi, M. Anpo, D.W. Bahnemann, *Chem. Rev.* 114 (2014) 9919–9986.
- [5] K. Sridharan, T.J. Park, *Appl. Catal. B: Environ.* 134 (2013) 174–184.
- [6] H. Cheng, B. Huang, Y. Dai, *Nanoscale* 6 (2014) 2009–2026.
- [7] Y. Xu, W. Zhang, *Appl. Catal. B: Environ.* 140 (2013) 306–316.
- [8] F. Amano, A. Yamakata, K. Nogami, M. Osawa, B. Ohtani, *J. Am. Chem. Soc.* 130 (2008) 17650.
- [9] J. Li, Y. Yu, L. Zhang, *Nanoscale* 6 (2014) 8473–8488.
- [10] S. Wang, D. Li, C. Sun, S. Yang, Y. Guan, H. He, *Appl. Catal. B: Environ.* 144 (2014) 885–892.
- [11] W. Shan, Y. Hu, M. Zheng, C. Wei, *Dalton Trans.* 44 (2015) 7428–7436.
- [12] S. Shamaila, A.K.L. Sajjad, F. Chen, J. Zhang, *Appl. Catal. B: Environ.* 94 (2010) 272–280.
- [13] X. Zhang, T. Guo, X. Wang, Y. Wang, C. Fan, H. Zhang, *Appl. Catal. B: Environ.* 151 (2014) 486–495.
- [14] J. Hu, G. Xu, J. Wang, J. Lv, X. Zhang, T. Xie, Z. Zheng, Y. Wu, *Dalton Trans.* 44 (2015) 5386–5395.
- [15] P. Niu, L. Zhang, G. Liu, H. Cheng, *Adv. Funct. Mater.* 22 (2012) 4763–4770.
- [16] J. Hong, X. Xia, Y. Wang, R. Xu, *J. Mater. Chem.* 22 (2012) 15006–15012.
- [17] J. Zhang, X. Chen, K. Takanabe, K. Maeda, K. Domen, J.D. Epping, X. Fu, M. Antonietti, X. Wang, *Angew. Chem. Int. Ed.* 49 (2010) 441–444.
- [18] J. Xu, H. Wu, X. Wang, B. Xue, Y. Li, Y. Cao, *Phys. Chem. Chem. Phys.* 15 (2013) 4510–4517.
- [19] X. Wang, K. Maeda, A. Thomas, K. Takanabe, G. Xin, J.M. Carlsson, K. Domen, M. Antonietti, *Nat. Mater.* 8 (2009) 76–80.
- [20] N. Cheng, J. Tian, Q. Liu, C. Ge, A.H. Qusti, A.M. Asiri, A.O. Al-Youbi, X. Sun, *ACS Appl. Mater. Interfaces* 5 (2013) 6815–6819.
- [21] X. Chen, J. Zhang, X. Fu, M. Antonietti, X. Wang, *J. Am. Chem. Soc.* 131 (2009) 11658.
- [22] X. Wang, X. Chen, A. Thomas, X. Fu, M. Antonietti, *Adv. Mater.* 21 (2009) 1609–1612.
- [23] J. Li, B. Shen, Z. Hong, B. Lin, B. Gao, Y. Chen, *Chem. Commun.* 48 (2012) 12017–12019.
- [24] X. Bai, L. Wang, R. Zong, Y. Zhu, *J. Phys. Chem. C* 117 (2013) 9952–9961.
- [25] C. Han, L. Ge, C. Chen, Y. Li, X. Xiao, Y. Zhang, L. Guo, *Appl. Catal. B: Environ.* 147 (2014) 546–553.
- [26] H. Li, L. Zhou, L. Wang, Y. Liu, J. Lei, J. Zhang, *Phys. Chem. Chem. Phys.* 17 (2015) 17406–17412.
- [27] J. Lei, Y. Chen, L. Wang, Y. Liu, J. Zhang, *J. Mater. Sci.* 50 (2015) 3467–3476.
- [28] J. Lei, Y. Chen, F. Shen, L. Wang, Y. Liu, J. Zhang, *J. Alloy Compd.* 631 (2015) 328–334.
- [29] K. Sridharan, E. Jang, T.J. Park, *Appl. Catal. B: Environ.* 142–143 (2013) 718–728.
- [30] L. Ge, C. Han, J. Liu, *Appl. Catal. B: Environ.* 108–109 (2011) 100–107.
- [31] F. Dong, Z. Zhao, T. Xiong, Z. Ni, W. Zhang, Y. Sun, W. Ho, *ACS Appl. Mater. Interfaces* 5 (2013) 11392–11401.
- [32] H. Jiang, J. Liu, K. Cheng, W. Sun, J. Lin, *J. Phys. Chem. C* 117 (2013) 20029–20036.
- [33] A. Nattestad, M. Ferguson, R. Kerr, Y.B. Cheng, U. Bach, *Nanotechnology* 19 (2008) 295–304.
- [34] Y. Wang, X. Wang, M. Antonietti, *Angew. Chem. Int. Ed.* 51 (2012) 68–89.
- [35] L. Ma, X. Xu, X. Zhou, *Chem. Lett.* 43 (2014) 947–949.
- [36] S. Anandan, G. Lee, P. Chen, C. Fan, J.J. Wu, *Ind. Eng. Chem. Res.* 49 (2010) 9729–9737.
- [37] H. Cheng, B. Huang, K. Yang, Z. Wang, X. Qin, X. Zhang, Y. Dai, *ChemPhysChem* 11 (2010) 2167–2173.
- [38] M. Xiong, L. Chen, Q. Yuan, J. He, S. Luo, C. Au, S. Yin, *Dalton Trans.* 43 (2014) 8331–8337.
- [39] L. Ye, J. Liu, Z. Jiang, T. Peng, L. Zan, *Appl. Catal. B: Environ.* 142 (2013) 1–7.
- [40] H. Gan, G. Zhang, H. Huang, J. Hazard. Mater. 250 (2013) 131–137.
- [41] J. Di, J. Xia, S. Yin, H. Xu, L. Xu, Y. Xu, M. He, H. Li, *J. Mater. Chem. A* 2 (2014) 5340–5351.
- [42] G. Zhang, J. Zhang, M. Zhang, X. Wang, *J. Mater. Chem.* 22 (2012) 8083–8091.
- [43] A. Thomas, A. Fischer, F. Goettmann, M. Antonietti, J. Mueller, R. Schloegl, J.M. Carlsson, *J. Mater. Chem.* 18 (2008) 4893–4908.
- [44] A. Vinu, P. Srinivasu, D.P. Sawant, T. Mori, K. Ariga, J. Chang, S. Jhung, V.V. Balasubramanian, Y.K. Hwang, *Chem. Mater.* 19 (2007) 4367–4372.
- [45] S. Liu, Y. Tu, G. Dai, *Ceram. Int.* 40 (2014) 2343–2348.
- [46] J. Cao, X. Li, H. Lin, S. Chen, X. Fu, J. Hazard. Mater. 239 (2012) 316–324.
- [47] S. Kumar, A. Baruah, S. Tonda, B. Kumar, V. Shanker, B. Sreedhar, *Nanoscale* 6 (2014) 4830–4842.
- [48] X. Wang, Q. Wang, F. Li, W. Yang, Y. Zhao, Y. Hao, S. Liu, *Chem. Eng. J.* 234 (2013) 361–371.
- [49] T. Surendar, K. Santosh, K. Syam, S. Vishnu, *J. Mater. chem. A* 2 (2014) 6772–6780.
- [50] S. Wang, D. Li, C. Sun, S. Yang, Y. Guan, H. He, *Appl. Catal. B: Environ.* 144 (2014) 885–892.
- [51] Z. Jiang, F. Yang, G. Yang, L. Kong, M.O. Jones, T. Xiao, P.P. Edwards, *J. Photochem. Photobiol. A* 212 (2010) 8–13.